7B.4. SUPERCELL POLARIMETRIC SIGNATURES AT X-BAND: DATA FROM VORTEX2

Christopher M. Schwarz* and Donald W. Burgess
Cooperative Institute for Mesoscale Meteorological Studies (CIMMS), The University of Oklahoma, Norman, OK

1. INTRODUCTION

Most dual-polarimetric (dual-pol) studies have been performed at S- and C-bands (e.g., Kumjian and Ryzhkov 2008, Romine et al. 2008, Ryzhkov et al. 2005a, Ryzhkov et al. 2002, Van Den Broeke 2008), but relatively few studies have been made at X-band. Certain signatures have been found to exist in supercell thunderstorms. These signatures include the tornado debris signature (TDS; Ryzhkov et al. 2002, 2005a), the low-level Z_{DR} arc (e.g., Kumjian and Ryzhkov 2008, 2009; Snyder 2008), Z_{DR} and K_{DP} columns (e.g., Caylor and Illingworth 1987; Hubbert et al. 1998; Loney et al. 2002; Kumjian and Ryzhkov 2008), midlevel Z_{DR} and ρ_{HV} rings (Kumjian and Ryzhkov 2008; Kumjian 2008), updraft signature (Kumjian and Ryzhkov 2008), and hail signatures (Heinselman and Ryzhkov 2006). Each signature reveals a distinguishing distribution of hydrometeors. Varying hypotheses have correlated these characteristics to different kinematic properties of the parent storm and its interaction with the environmental flow. However, attenuation $A_{H,V}$ and differential attenuation A_{DP} are problematic at X-band. Using results from Snyder et al. (2010), the ZPHI Rain-Profiling algorithm (Testud et al. 2000), and the "Gamma" method (e.g., Bringi et al. 1990) are used to correct for A_H and A_{DP}, respectively.

This paper gives a general overview of the observations and evolution seen at X-band (3-cm) wavelength. The main focus is to provide a summary of storm evolution obtained from the NOAA (NSSL) X-Band Polarized (NOXP) mobile weather radar during the **V**erification of the **OR**igins of **T**ornadoes **EX**periment, Part 2 (VORTEX2) field project. Herein, the hail signature, Z_{DR} arc, and Z_{DR} and K_{DP} column signatures and evolution are analyzed in correspondence to the evolution of the updraft signature from three supercells; one tornadic (5 June 2009), one nontornadic (7 June 2009), and one cyclic, tornadic (10 May 2010).

2. METHODOLOGY

2.1. *Data Collection*

For eleven and ½ weeks during the springs of 2009 and 2010, NOXP collected data during the VORTEX2 field campaign. NOXP collected data as a mesocyclone-scale radar (a radar assigned to scan the low- to mid-level regions of the storm at relatively close range (5-30 km)).

The radar provided dual-pol observations and radial velocities for dual-Doppler in association with other mesocyclone-scale radars (two Doppler on Wheels: (DOW6 and DOW7) and UMass X-Pol (UMXP)). Table 1 details NOXP specs for 2009 and 2010. The advantage of this mobile radar is high spatial resolution and fast updates. During all three days analyzed in this paper, NOXP performed two-minute time syncs. The scanning strategies are listed in Table 1.

Name	NOXP
Type	X-Band (λ≈3.21 cm)
Frequency	9410 MHz
3-dB Beamwidth	1.0°
Effective Beamwidth	~1.45°
Azimuthal Sampling Rate	0.5°
Antenna Rotation Rate	28-29° sec^{-1}
Peak Power	200 kW
Processor	Sigmet RVP8
Pulse Repetition Frequency (PRF) /Nyquist Co-Interval	**2009: Low Res.:** ~950 Hz / +/- 7.6 m/s **High Res.:** ~1700 Hz/ +/- 13.6 m/s **2010:** ~2500 Hz/ +/- 20 m/s
Gate Spacing	**2009: Low Res.:** 150 meter **High Res.:** 75 meter **2010:** 75 meter
Max Unambiguous Range	**2009: Low Res.:** 158 km **High Res.:** 88 km **2010:** 60 km
Number of Samples	**2009: Low Res.:** 32 **High Res.:** 60 **2010:** 40
Scanning Strategy (Elevations collected)	**2009: Low Res.:** 0.5°-8.5° (1° interval) (120° sector scans) **High Res.:** 0.5°, 1.0°-11.0° (1° interval) (120° sector scans) **2010:** 1°-7° (1° interval) (360° full scans)

Table 1 – Specifications for the NOXP mobile weather radar during VORTEX2.

In 2009, low-resolution data were required for a few minutes during initial deployment to allow for transmitter warm up, followed by high-resolution data for the remainder of the deployment. Low Resolution velocity data were deemed unrecoverable due to the low Nyquist co-interval. In 2010, after adjustments to the transmitter a higher Nyquist co-interval was achieved, resulting in better velocity data.

2.2. *Data Preparation*

* *Corresponding author address:* Christopher Schwarz, University of Oklahoma, School of Meteorology, 120 David L. Boren Blvd., Rm. 4340D Norman, OK 73072-7307; email: cmschwarz@ou.edu

The NOXP data were first de-cluttered and de-aliased (if possible) using Solo II (Oye et al. 1995) and heading corrections were performed. The data were converted from DORADE Sweep files to NetCDF format using the Foray translator. Attenuation corrections were made using a program written by Jeff Snyder for work in Snyder et al. (2010). For more information about the program, the reader is deferred to Snyder (2008). Factors affecting the technique are discussed in Section 3.

A 3-Dimensional Barnes 2-pass objective analysis scheme (Barnes 1964; Koch et al. 1983; Majcen et al. 2008) was implemented for the moment and polarization data for each case. The smoothing parameter, κ_0, is calculated using Pauley and Woo (1990), based on the coarsest data separation in the data set. A constant convergence parameter, γ, of 0.3 was used for every case as suggested in Majcen et al. (2008). Storm propagation was not accounted for in the objective analysis for the 2009 cases, but was for the 2010 case due to fast storm motion. In some cases, Constant Altitude Plan Position Indicators (CAPPIs), Range Height Indicators (RHIs), and vertical cross-sections were obtained using the *Vis5d* (ftp://ftp.ssec.wisc.edu/pub/vis5d-5.2/README) visualization software. All height calculations in the objective analysis are calculated using equation 2.28b from Doviak and Zrnic (1993) (i.e. the 4/3's earth's radius rule). Dual-Doppler wind syntheses are calculated by integrating the anelastic continuity equation upward by setting w=0 at the surface. The wind synthesis package was developed for work in Ray et al. (1980).

3. HYDROMETEOR IMPACTS ON SIGNAL

3.1. *Attenuation: A_H and A_{DP}*

Reflectivity factor $Z_{H,V}$ and differential reflectivity factor Z_{DR} at shorter wavelengths (such as X-band), are more prone to signal loss, or attenuation. Attenuation is more prevalent when hydrometeor diameters become comparable to radar wavelength. Hydrometeor type, number concentration, and distribution within the resolution volume all contribute to attenuation. Significant attenuation ($A_{H,V}$) (subscripts H and V denote the horizontally and vertically polarized waves) often results from liquid hydrometeors rather than ice hydrometeors owing to the higher dielectric factor of water. Similarly, specific differential attenuation (A_{DP}) is given by: A_{DP}=A_H - A_V. Unattenuated reflectivity factor $Z'_{H,V}$ (dBZ) and differential reflectivity factor Z'_{DR} can be obtained by adding the two-way path integrated attenuation $PIA_{H,V}$ (dBZ km^{-1}) and differential attenuation PIA_{DP} (dB km^{-1}) (Bringi and Chandrasekar 2001) down a radial to the measured $Z_{H,V}$ and Z_{DR}, respectively.

Differential phase data (both specific (K_{DP}: e.g. Bringi et al.1990; Park et al. 2005) and ϕ_{DP}: (Testud et al. 2000; Ryzhkov and Zrnic 1995; Bringi et al. 2001)) have been tested in different relationships to mitigate A_H and A_{DP}. K_{DP} is simply the range derivative of ϕ_{DP}. However, K_{DP} tends to be noisy in the presence of resonance scatterers i.e. backscatter differential phase δ. Extraction of accurate ϕ_{DP} from Φ_{DP} (related as: $\Phi_{DP} = \phi_{DP} + \delta$ (Bringi and Chandrasekar 2001)) requires removal of δ as it contributes to large Φ_{DP} initially or at the end of an echo down a radial. The iterative method requires removal of δ at either edge of the echo. This is not always possible and limits attenuation recovery calculations.

3.2. *Attenuation Corrections*

The ZPHI algorithm (Testud et al. (2000)) constrains path-integrated attenuation by the total change in ϕ_{DP} along a radial through a rain cell. An iterative filtering and smoothing method (2 km range) extracts ϕ_{DP} from Φ_{DP} (Hubbert and Bringi 1995). However, hail presents a challenge for attenuation estimates, as the fractional water content heavily influences attenuation. ZPHI requires the exponent (b) in the $A_H - Z_H$ relation as defined in Hitschfeld and Bordan (1954). Another required coefficient is α_H in the $A_H - K_{DP}$ relation (Bringi et al. 1990; Jameson 1992; Park et al. 2005a). α_H varies greatly as a function of the DSD, temperature, and drop shape relation. Different studies using disdrometer data have found varying values for α_H for X-Band (e.g. Bringi et al. 1990; Matrosov et al. 2002; Jameson 1991; Zhang 2008 (*personal communication*); Park et al. 2005a). (α_H = 0.32; b = 0.722) were chosen for the corrections used in this study, however holding α_H constant is not a good assumption in areas of large raindrops (Ryzhkov and Zrnic 2005).

In regions of total attenuation the ZPHI technique does not work, as there is no change in ϕ_{DP} down the radial. Hitschfield and Bordan (1954) found $A_{H,V}(r)$ at all locations between r and r_0 may be calculated by

$$A_{H,V}(r) = \frac{Z^b_{H,V}(r)\left\{10^{0.1b\alpha\Delta\phi_{DP}} - 1\right\}}{I(r,r_0) + \{10^{0.1b\alpha\Delta\phi_{DP}} - 1\} I(r,r_0)} \qquad (1)$$

where the I (Testud et al. 2000) is the path integral down a ray, r is the beginning range of the ray, r_0 is the ending range of the cell, and where $\Delta\phi_{DP} = \phi_{DP}(r_1) - \phi_{DP}(r_0)$.

To correct A_{DP}, the ZPHI algorithm allows for the estimation of the normalized slope parameter N_0^* (see their paper for more details) down a radial. However, A_{DP} was believed to be underestimated using ZPHI, thus the "Gamma" method (e.g., Snyder et al. 2010) is used for 2010 corrections. The Gamma method utilizes the linear relationship between K_{DP}, A_H, and A_{DP} (Bringi et al. 1990). A_{DP} is estimated as

$$A_{DP} = \frac{\alpha_{DP}}{\alpha_H} A_H = \gamma A_H \qquad (2)$$

where α_{DP} and α_H are 0.0.0483 and 0.313, respectively (Cao et al. 2008; Cao and Zhang 2009; Snyder et al. 2010).

3.3. RESONANCE IMPACTS

Resonance (Mie) scattering occurs for different diameters of differing hydrometeor type, and increases for shorter wavelengths. Barring attenuation, resonance impacts cause an oscillation in the amount of backscatter signal that the radar receives. However, resonance at X-band is less than C-band due to increased attenuation. Since $Z_{H,V}$ and Z_{DR} are a measure of the returned signal, their measurements oscillate as well. δ increases in the presence of resonance scattering, which can directly lead to highly negative K_{DP} values, and ρ_{HV} naturally is lower than 1.0 in a pure rain regime. For very large hydrometeors, ρ_{HV} can yield very low values.

Rayleigh scattering occurs for diameters D < λ/16, or more accurately by D=($\lambda\Re$)/(|ε|)$^{1/2}$ (Kumjian 2008; Kumjian et al. 2008) where $\Re\approx$ 1.0, 1.5, 2.0, 2.5, etc., |ε| is the dielectric constant, and λ is the radar wavelength. As $\Re$ increases the impacts decrease due to increasing attenuation (Kumjian 2008). For X-band, resonance scattering occurs around ~2 mm sized raindrops. Although, differing dielectric properties of water and ice yield different fluctuations of scattering, hail resides in the resonance regime. Increases of liquid water on hail will increase attenuation, which has a dampening effect on resonance scattering (Snyder 2008).

4. 5 JUNE 2009

On 5 June 2009 the VORTEX2 armada intercepted a tornadic supercell in Goshen County, Wyoming. The tornado developed at ~21:55 UTC (all times hereafter are UTC) as NOXP was in transit to a deployment spot. Data collection began with a low-res. scan at 22:16:09 around the peak intensity time of the tornado. High-res. data collection began at 22:22:17 and ended at 22:43:47. Local soundings indicate that the environmental melting level is ~4.25 km above sea level (ASL) (~2.57 km above radar level (ARL)). The in-cloud melting layer, away from the updraft region is observed to be ~3.1 km ASL (~1.47 km ARL).

4.1. *Tornadic Debris Signature*

From ~22:16 to ~22:24, the tornado is seen as a Z_H depression (~30 dBZ). This depression coincides with a tornadic vortex signature (TVS), which is evident in the 1° elevation plan position indicator (PPI) at ~22:22 (Fig. 1). High Z_H (~51 to ~57 dBZ) surround the tornado's location above ~1.0 km ARL, which is thought to be associated with the tornado debris signature (TDS).

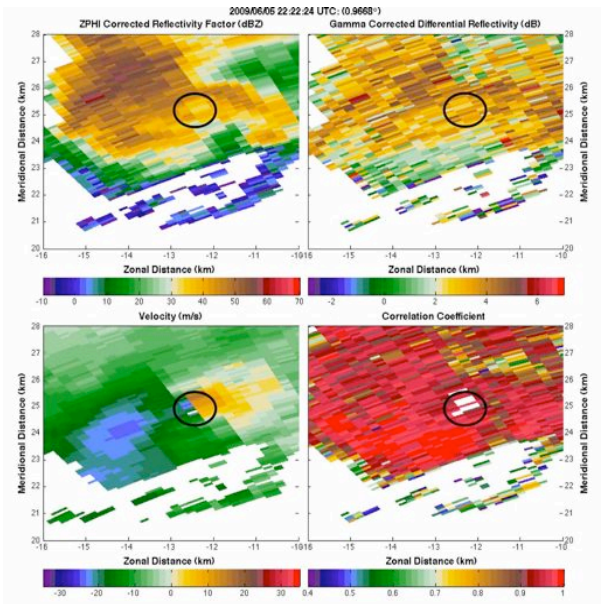

Fig. 1 – PPI at 22:22:24 at 1.0° elevation of Z_H (top left), Z_{DR} (top right), V_r (bottom left), and ρ_{HV} (bottom right) illustrating the possible TDS. Annotated is the location of the TVS.

The tornado was rain-wrapped initially, but was more visible by this time. ρ_{HV} drops out in the location of the TVS, likely because of noise caused by randomly oriented debris and Z_{DR} reduces slightly to ~2.0 dB. This makes the TDS difficult to discern. This signature disappears by 22:24 and the velocity couplet disappears at ~22:30:21 coinciding with the full dissipation of the tornado. However, a region of remnant weak shear remains.

4.2. *Updraft Signature*

As noted before in previous literature, updraft signatures are often characterized by reductions of ρ_{HV}, collocated Z_H reduction regions, and flanking Z_{DR} columns. It has been speculated that lower ρ_{HV} may be an indirect measure of updraft strength (Ryzhkov et al. 2005; Kumjian 2008). Variable factors such as light particulate matter (dust, insects, grass, leaves, etc.) lofted in inflow at lower-levels could reduce ρ_{HV}. Aloft, additional possibilities include sparse large irregularly shaped hail, tumbling hail, mixed unfrozen and frozen particles, or a low number concentration of hydrometeors (Kumjian 2008; Kumjian et al. 2010), all of which will substantially reduce ρ_{HV}.

Early on in the deployment (22:16:09 - ~22:22) a series of updraft pulses (A1 – A3; Fig. 2) are observed along the hook echo and along the surging rear-flank gust front (RFGF) as annotated in Fig. 2. This is verified in dual-Doppler data between NOXP and the Doppler-on-Wheels 6 (Fig. 3). The width of the low-level WER suggests a broad region of rising motion. Varying horizontal and vertical extent of BWERs suggests that

these pulses of updraft vary in magnitude, and are embedded within a larger region of updraft. The heights of the BWERs are seen to rapidly fluctuate on time scales shorter than that observed by the radar. Another region of rising motion is observed along a secondary gust front, which is associated with updraft pulse B1 (Fig. 2).

Examining CAPPIs of the same regions with ρ_{HV}, one can identify roughly the same locations as updraft (Fig. 2). The reduction of ρ_{HV} is dependent on the number concentration and particle type, i.e. signal-to-noise ratio (SNR) biases ρ_{HV} in a BWER without scatterers.

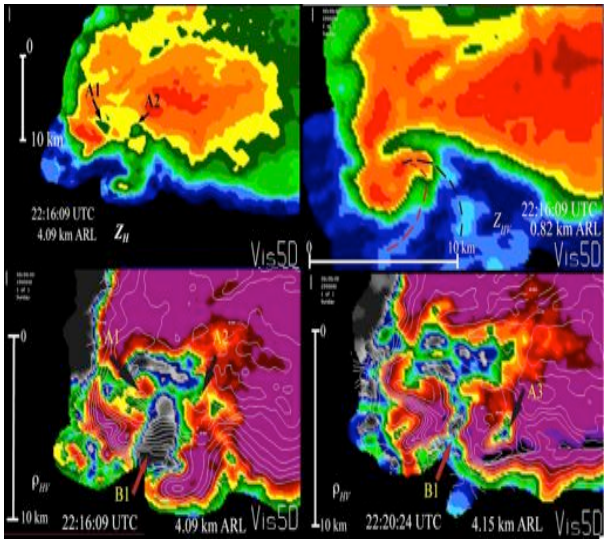

Fig. 2 – CAPPIs of (top left) Z_H from 22:16:09 at 4.09 km ARL annotating A1 & A2, (top right) Z_H from 22:16:09 at 0.82 km ARL annotating the gust fronts, (lower left) ρ_{HV} from 22:16:09 at 4.09 km ARL annotating A1, A2, and B1, and (lower right) ρ_{HV} from 22:20:24 at 4.15 km ARL annotating B1 & A3. See Table 2 in Appendix A for color scale.

Within the reduction regions, one must consider vertical and horizontal trajectories of hydrometeors. This includes descending ice hydrometeors or supercooled liquid drops and advection within and exiting the updraft.

The anomalously low ρ_{HV} (Fig. 2) are characterized by extremely variable values of Z_{DR} (-0.6 - ~3.5 dB), and Z_H values between ~30 to ~43 dBZ. Reductions in ρ_{HV} and Z_{DR} near the updraft could be the result of large irregularly shaped or tumbling hail, whereas the region farthest from the updraft center could be advection of graupel around the north side of the updraft. Intense updrafts have more intense divergence signatures aloft, which can carry smaller particles with lower terminal velocities farther. Furthermore, it should be noted that Z_{DR} is biased by noise down radial from the hook region as seen in regions of strong A_H and A_{DP}. Optimal SNR values for adequate ρ_{HV} measurements at X-band are still being investigated.

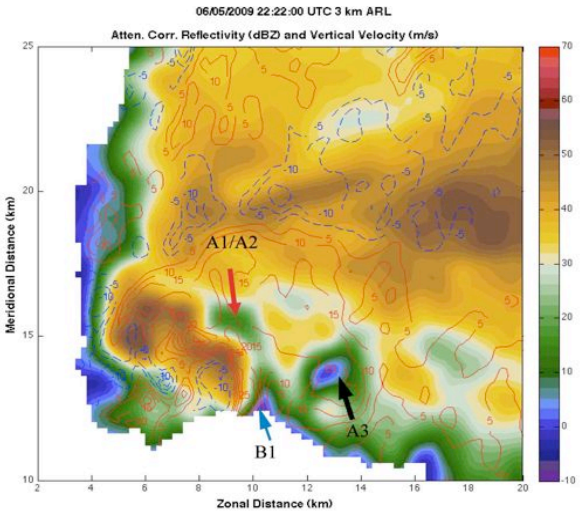

Fig. 3 – CAPPI of dual-Doppler vertical velocities (w) overlaid on Z_H taken from 22:22 at 3 km ARL. Red contours are positive w every 5 m/s, and blue dashed contours are negative w every 5 m/s. Arrows indicate the location of the updraft pulses seen in Fig. 2.

Updraft pulses A1, A2, and B1 appear to weaken as the BWER diminishes in the 22:24:05 – 22:26:04 time frame (Fig. 4). The BWER and dual-pol characteristics associated with A3 persist as a new updraft pulse A4 is observed (Fig. 4) at 5.11 km ARL around 22:26:04. Negative K_{DP} at 22:24 indicates the likelihood of resonance-sized scatterers around the updraft region. This is likely associated with hail, which will be discussed later. By 22:30:05, the height of A3's BWER is diminishing, but A4 appears to increase in intensity by 22:32:04. Anomalously low ρ_{HV} (<0.4) curve cyclonically from the updraft region (Fig. 5) as shown at 22:32, which is likely associated with low SNR given the low Z_H in that region.

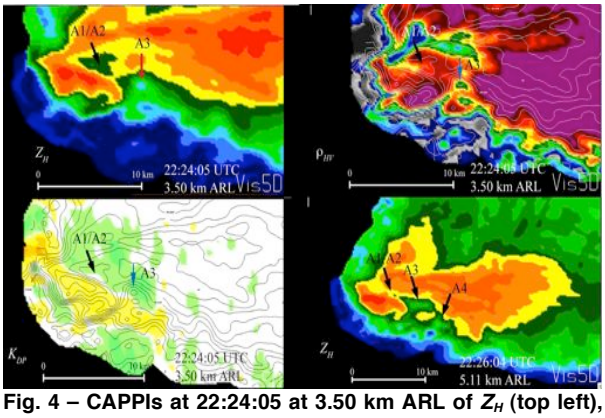

Fig. 4 – CAPPIs at 22:24:05 at 3.50 km ARL of Z_H (top left), ρ_{HV} (top right), and K_{DP} (lower left) with A1-A3 annotated (black and blue arrows). A4 is annotated in Z_H (lower right) as seen at 5.11 km ARL. See Table 2 in Appendix A for color scale.

For the remainder of the deployment, updraft pulse A4 persists, as the RFGF continues to surge around the low-level mesocyclone. Around 22:38:04, a new BWER

is evident in Z_H and reductions of ρ_{HV} suggest the presence of another updraft pulse A5 (Fig. 5). Similar, to the previous updraft pulses, this flanks the region of A4. The close spatial proximity of these pulses often makes it difficult to determine if these are extensions of each other, or separate pulsing centers.

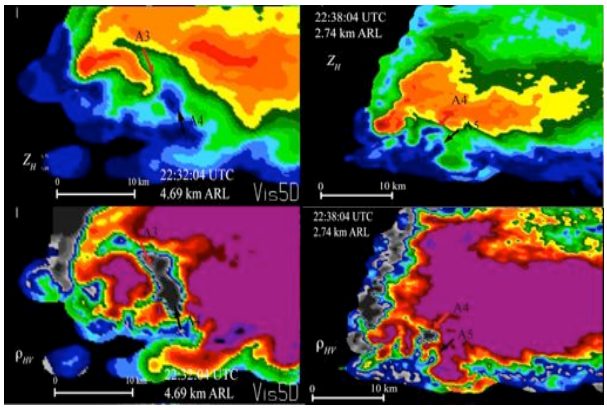

Fig. 5 – CAPPIs from 22:32:04 at 4.69 km ARL of Z_H (top left) and ρ_{HV} (bottom left) with A3 & A4 annotated (red and black arrows). CAPPIs from 22:38:04 at 2.74 km ARL of Z_H (top right) and ρ_{HV} (bottom right) with A4 & A5 annotated (red and black arrows). See Table 2 in Appendix A for color scale.

4.3. Z_{DR} Column and K_{DP} Column

The height of the Z_{DR} column is a useful indicator of the height of the updraft perturbed melting layer, as the column can extend several kilometers above the in-cloud melting layer outside of the updraft region. Supercooled drops are observed in the column above the in-cloud melting layer. This region is dominated by a small concentration of large raindrops (> 2 mm), a few-water coated hailstones, and low concentration of small-drops as confirmed by aircraft penetrations in Brandes et al. (1995) and Loney et al. (2002). At the periphery of the updraft where the magnitude of the vertical velocity diminishes, the largest raindrops and coated hailstones begin to fall, enhancing Z_{DR} (Kumjian and Ryzhkov 2008). This coincides with findings of Conway and Zrnic (1993) and Loney et al. (2002). K_{DP} columns, however, are generally offset from Z_{DR} columns in supercells due to environmental wind shear (Hubbert et al. 1998; Loney et al. 2002; Kumjian et al. 2008). K_{DP} columns have been found to be associated with a high concentration of liquid water, i.e. supercooled raindrops above the melting layer, raindrops, wet graupel, or liquid coated hail (Loney et al. 2002).

Vertical cross-sections taken between 22:16:09 and 22:20:24 indicate a tall Z_{DR} column on the north flank of the updraft region (Fig. 6). The close spatial proximity of updraft pulses A1 and A2, make correlating this Z_{DR} column difficult. Values of $Z_{DR} > 5.0$ dB and < 6.5 dB are seen up to ~4.6 km ARL. Magnitudes of the column fluctuate throughout the time period between 22:18 and 22:20. Blue arrows in Fig. 6 indicate high Z_{DR}, which is believed to be an artifact from low SNR in a region of significant attenuation. After, ~22:20 to ~22:24, there is a more substantial decrease in the height and weakening of the Z_{DR} column.

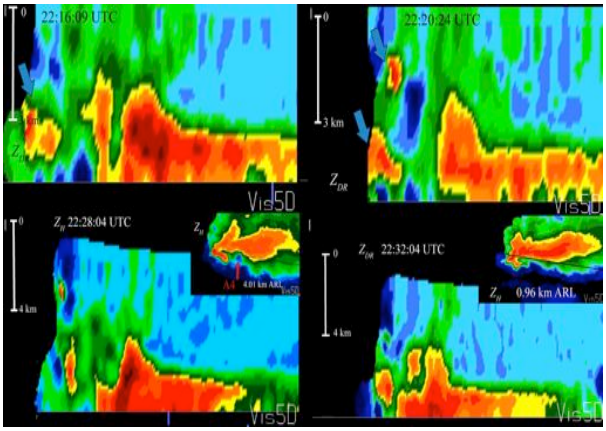

Fig. 6 – Z_{DR} column on the northern flank of updraft A1/A2 at 22:16:09 (top left) and 22:20:24 (top right). Blue arrows indicate anomalously high Z_{DR} that is non-meteorological. Columns at 22:28:04 (bottom left) and at 22:32:04 (bottom right) are seen to flank the region of continued updraft pulses. See Table 2 in Appendix A for color scale.

A well-defined Z_{DR} column has formed at 22:26:04 between the region of A3, and the developing pulse A4. Values in the column are now ~6.5 dB. At 22:28, a new column has developed in the same general vicinity as the previously mentioned column (Fig. 6). This column persists through the end of data collection, while another column develops around 22:38 flanking updraft A5. Uncertainty remains as to the correlation of these columns to their parent updraft pulses given the close spatial proximity of these pulses of updraft. A decrease in maximum Z_{DR} from ~6.5 dB to around 5.0 dB occurs prior to 22:37:47.

No traditional K_{DP} columns seem to exist in any location at this time other than the southern tip of the hook, where there is believed to a high liquid water content. This is likely due to the presence of significant δ occurring in a broad region surrounding the Z_{DR} column. Values often fluctuate in this region due precipitation advection around the hook and changes in updraft pulses.

A secondary column of enhanced K_{DP} develops in and around the BWER associated with updraft A4/A5 at 22:36:04 (Fig. 7). The large values aloft diminish after this time, but the two “column” regions remain through the rest of data collection.

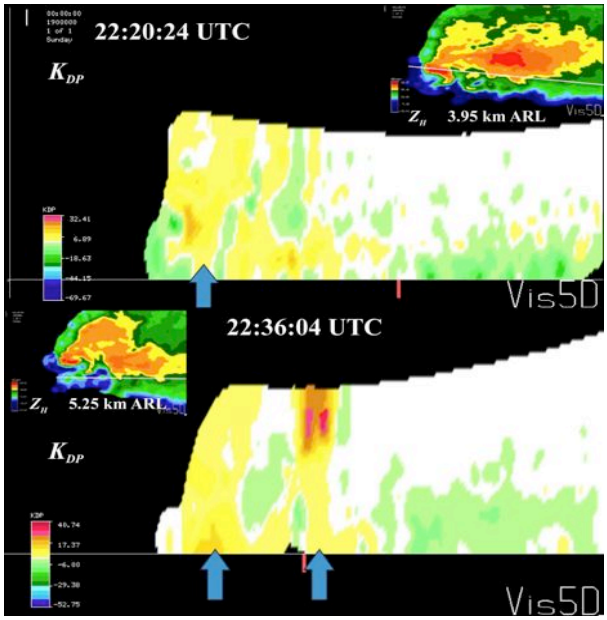

Fig. 7 - Columns of enhanced K_{DP} (denoted by blue arrow) in the hook region at 22:20:24 (top) and the secondary column from weak echo at 22:36:04 (bottom). Inset is a Z_H CAPPI at 3.95 km ARL (top) and 5.25 km ARL (bottom) denoting the location of the vertical slice. The height of volume at this location is ~6.0 km. See Table 2 in Appendix A for color scale.

4.4. *Hail Signature*

Larger hail yields a unique signature that has been noted to have higher Z_H, ≤0.80 ρ_{HV}, and ~0 dB Z_{DR} at S band (e.g., Heinselman and Ryzhkov 2006). Prior to the start of NOXP data collection, an NSSL Mobile Mesonet (Probe) reported 6.99 cm (2.75 in.) hail just north of the hook at 22:12:34, which lasted more than 10 min. The exact location of this report is unknown because of data loss associated with the loss of the windshield, thus knocking the vehicle out of commission for the rest of the deployment. NOXP data at 22:16:09 (Fig. 9) show a hail signature that spans the middle of the forward flank core (FFC), the rear flank core (RFC) region, and the northern hook region. This signature is defined by a reduction in ρ_{HV} (generally from ~0.4 to ~0.85), variable Z_H (~37 to ~65 dBZ), negative K_{DP} (from significant δ), and Z_{DR} between <0 - ~2.5 dB. The attenuation correction retrieves much of the FFC region, and shows that this signature extends through the highest Z_H regime.

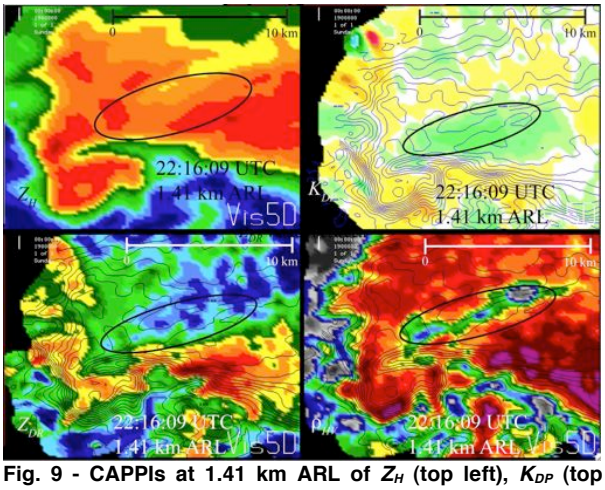

Fig. 9 - CAPPIs at 1.41 km ARL of Z_H (top left), K_{DP} (top right), ρ_{HV} (bottom left), and Z_{DR} (bottom right) at 22:16:09. The ellipse outlines the narrow corridor where hail is located. Note the negative K_{DP}, low ρ_{HV}, moderate Z_H, and low Z_{DR} associated with larger hail. See Table 2 in Appendix A for color scale.

Fluctuations of these values are thought to be associated with varying number concentration, varying diameters, and varying composition. However, care must be taken in certain regions due to non-uniform beam filling (NBF) (Ryzhkov 2007) effects.

As mentioned before, this ρ_{HV} and Z_{DR} reduction corridor is seen aloft, but it is also seen down low indicating vertical continuity as seen in the RHI at 22:16:09 in (Fig. 10).

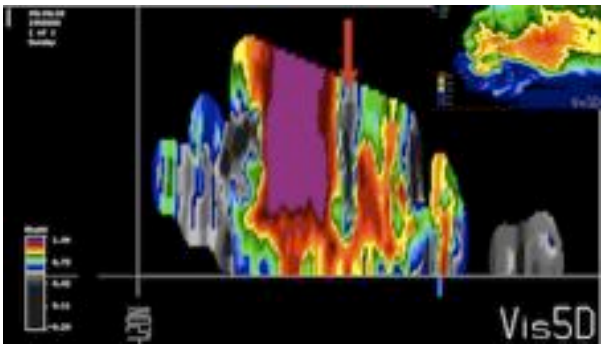

Fig. 10 – Vertical cross-section of ρ_{HV} illustrating the reduction regime due to hail (red arrow). Inset is a Z_H CAPPI taken at 0.42 km ARL at 22:16:09. The max height of the RHI is ~7.65 km ARL. See Table 2 in Appendix A for color scale.

ρ_{HV} decreases between ~22:18 and ~22:22, which could be associated with the descent of hail. This coincides with pulses A1, A2, and A3. Given the close spatial proximity to the A1/A2 region, it is plausible that these pulses could have either led to or assisted in the hail growth. At 22:17:15 Probe 3 reported 4.45 cm (1.75 in.) hail falling just north of the hook on the southern end of the RFC region. Fluctuations in height (between ~1.4 and ~2.0 km ARL) of ρ_{HV} <0.4, occurs between ~22:18 and ~22:22. It remains unclear as to the true value of

ρ_{HV} in the attenuated FFC region, but there is a possibility of smaller liquid coated hail and/or large raindrops in this region of the core. This is inferred from the amount of A_H and A_{DP} in this region.

Around 22:22:41 Probe 7 reported 4.45 cm (1.75 in.) hail mixed with rain in the vicinity of the radar hail signature. At this time ρ_{HV} is ~0.70 to ~0.75 in this vicinity, which is possibly due to the descent of hail. Liquid coated hail is thought to be contributing to the significant attenuation identified in CAPPIs at ~0.96 km at 22:26:04 and at ~1.60 km ARL at 22:28:04 (Fig. 11).

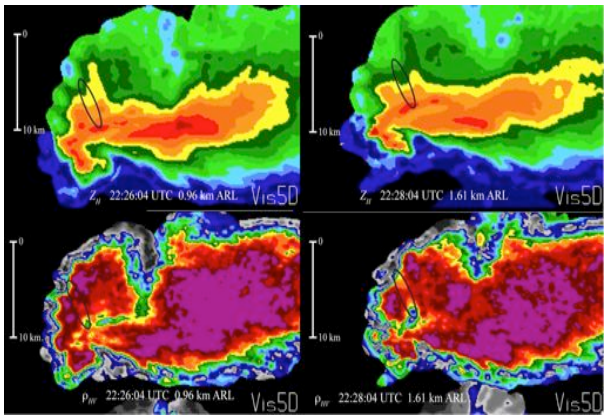

Fig. 11 - Region of significant attenuation in Z_H and ρ_{HV} indicated with the ellipses. The CAPPIs are at 22:26:04 (left) and 22:28:04 (right) at 0.96 km ARL (left) and 1.61 km ARL (right) in height. See Table 2 in Appendix A for color scale.

After 22:39:47, the extent of the ρ_{HV} reduction only occurs north of the hook, and low-level reductions of ρ_{HV} diminish. This and the increase in A_{DP} at low-levels indicate more liquid precipitation and/or smaller hail sizes as the dominant precipitation type.

4.5. Z_{DR} Arc Evolution

The Z_{DR} arc is known to be common to supercells around the world (e.g. Höller et al. 1994; Outinen and Teittinen 2007; Kumjian and Ryzhkov 2008; Kumjian 2008; Van Den Broeke 2008). This signature is found along a Z_H gradient on the inflow side of the storm below the melting level. Kumjian and Ryzhkov (2008, 2009) theorize that the Z_{DR} arc is a product of size sorting from impacts of Storm Relative Environmental Helicity (SREH; Davies Jones et al. 1990). There is a Z_{DR} arc defined by values up to ~6.5 dB initially at 22:16:22 (Fig. 12), which elongates by 22:17:37, and then begins to weaken at 22:18:55. This weakening in the arc could be associated with updraft A3 lofting the sparse large hydrometeors believed to be present in the arc region (Kumjian and Ryzhkov 2008; Kumjian 2008). This could easily reduce the values in the arc region.

Between ~22:24 - ~22:26, no arc is present with the higher Z_{DR} values extending into the forward core region. Z_{DR} values increase in the southern region of the forward flank, which is seen spanning across a gradient of Z_H. Also, the northern flank of Z_{DR} (note the two arrows in Fig. 12, lower left) divides into two "branches" in the FFC region, which merge by 22:28:04 (Fig. 12). The mechanism for this remains unclear, but perhaps this is related to the oscillations of the Z_{DR} arc and its relationship with the cycles of updrafts. More investigation is required.

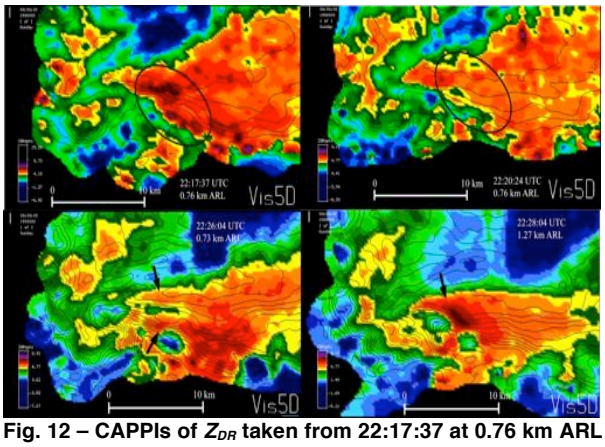

Fig. 12 – CAPPIs of Z_{DR} taken from 22:17:37 at 0.76 km ARL (top left), 22:20:24 at 0.76 km ARL (top right), 22:26:04 at 0.73 km ARL (lower left), and 22:28:04 at 0.73 km ARL (lower right) that illustrate the evolution of the Z_{DR} arc (annotated with black ellipses and arrows). Note the fluctuations in the magnitude of the arc. See Table 2 in Appendix A for color scale.

At ~22:28, the arc's values increase to around ~6.0 to ~6.5 dB. The height of the arc region extends to 1.36 km, and is likely enhanced by the presence of the updrafts A3 and A4. Size sorting due to vertical velocities should not be ruled out as a contributing factor to the distribution of the largest drops. At 22:30:05 larger drops are distributed along the entire length of the inflow side of the echo. However, falling precipitation leads to rapid fluctuations that are under sampled in the two-minute time syncs.

By 22:32:04 high Z_{DR} values have descended to near the surface in the arc region as values above 0.37 km ARL diminish as seen in (Fig. 13). In the 22:34:17 volume the arc has become disorganized and evolved into a "divided" appearance again. It is speculated that environmental winds advect hydrometeors (both water and ice) that are lofted in the updraft region A4/A5. This redistributes precipitation to the eastern edge of the forward flank, which is seen up to ~2.0 km in height. Below this height Z_{DR} increases, indicating the hydrometeor fallout. No Z_{DR} arc occurs in the remaining times of data collection. However, this does not rule out the possibility of reorganization following the increase in the low-level circulation at 22:42:04.

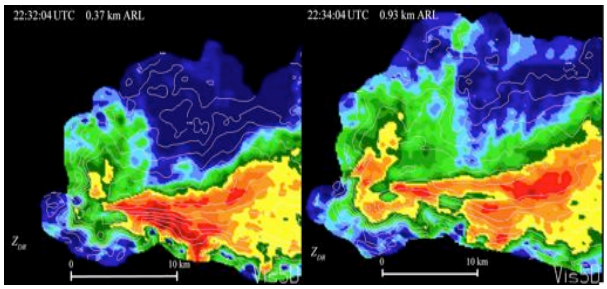

Fig. 13 - CAPPIs illustrating the redistribution of the Z_{DR} arc taken from 22:32:04 (left) at 0.37 km ARL and from 22:34:04 at 0.93 km ARL. Z_H (white contours) is contoured every 5 dBZ. See Table 2 in Appendix A for color scale.

5. 7 JUNE 2009

On 7 June 2009, NOXP's first deployment was east of Oregon, MO. The supercell was initially non-tornadic, but later produced a brief tornado during a second, shorter deployment. The radar's high-res. scans ran from 23:42:07 to 00:03:48. The storm initially had a more classic look to it, but around ~23:48, the hook became very ragged as the storm transitioned to an outflow dominant high precipitation storm. It should be noted that the storm was in very close proximity to the radar, and this limited the height to which the radar was scanning. Local soundings indicate that the environmental melting layer is ~4.0 km ASL, and the in-cloud melting layer is ~2.94 km ARL.

5.1. *Updraft Signature*

Given the shallow depth of data, all updraft analyses are limited to analyses of the ρ_{HV} reduction signatures that have vertical continuity. Two updraft signatures (updraft A & B) are observed at 23:42:07 and 23:46:04, respectively (identified with blue (A) and red arrows (B) in Fig. 14) along the inflow side of the hook region. The updraft signatures show a very narrow gradient between the updraft and downdraft area. The two are identified by substantial reductions of ρ_{HV} (down to ~0.68), low Z_H (~30 - ~35 dBZ), and variable Z_{DR} (~0.5 - ~3.5 dB). The updraft signatures are thought to be associated with a mixture of light debris and sparse large hail. At 23:50:04 there appears to be evidence of a new updraft (updraft C) further northeast along the forward flank core (FFC) region as seen in the polarimetric variables (Fig. 15).

Between 23:50 and 23:56, a descending reflectivity core (DRC) is observed in the region of C (black ellipse in Fig. 16). The DRC is characterized by ~5 – ~45 dBZ, Z_{DR} (~5.0 - ~6.5 dB), and ρ_{HV} (between ~0.73 and ~0.90) (all values increase with height). ρ_{HV} increases to ~0.99 by 23:56:04, and Z_{DR} increases to values between ~4.5 - ~7.0 dB. This could be from larger hydrometeors descending off of the updraft, or the weakening of updraft in this region. At 23:54:04, a new updraft region (pulse D) to the northeast of the DRC is seen in CAPPIs in Fig. 16.

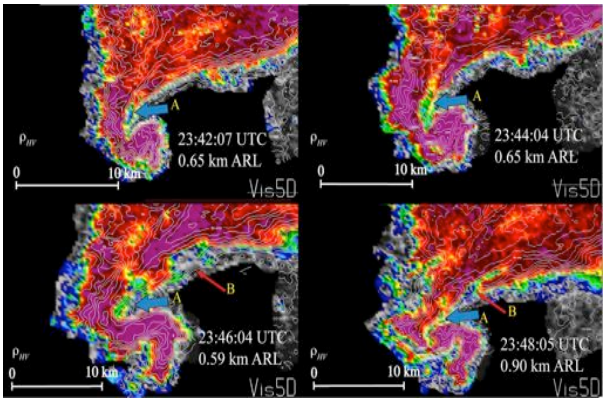

Fig. 14 – CAPPIs of ρ_{HV} reduction regions in updraft locations (indicated by arrows) at 23:42:07 (top left) at 0.65 km ARL, 23:44:04 (top right) at 0.11 km ARL, 23:46:04 (bottom left) at 0.59 km ARL, and 23:48:05 (bottom right) at 0.90 km ARL. Overlaid are Z_H contours in white plotted every 5 dBZ. See Table 2 in Appendix A for color scale.

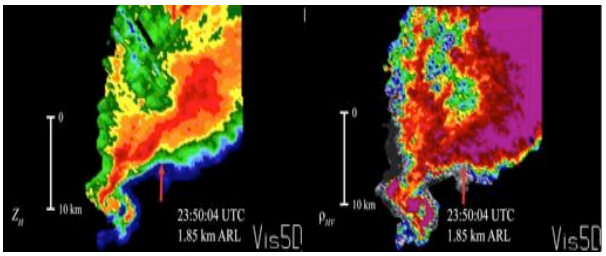

Fig. 15 - CAPPIs of Z_H (left) and ρ_{HV} (right) at 23:50:04 at 1.85 km ARL. See Table 2 in Appendix A for color scale.

At 23:58:04, this updraft region appears to weaken as its diameter is diminishing, and the region is becoming filled with precipitation. Hereafter the eastern extent of the echo moves out of the sector. Also, the close proximity to the radar and propagation make evidence of cyclic updrafts difficult to determine.

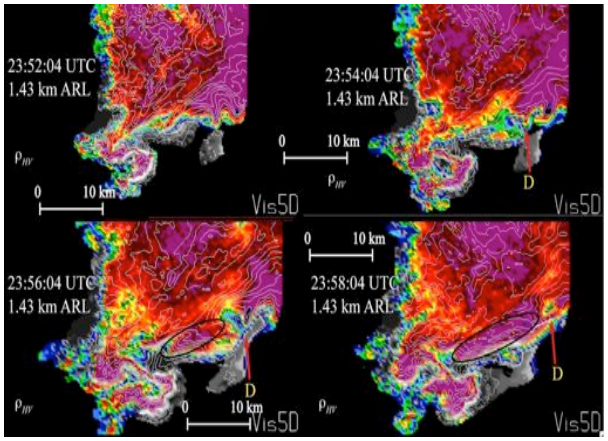

Fig. 16 – CAPPIs of ρ_{HV} at 1.43 km ARL. The times are 23:52:04 (top left), 23:54:04 (top right), 23:56:04 (bottom left), and 23:58:04 (bottom right). Updraft D is denoted with the red arrow. Black ellipse denotes the DRC in updraft pulse C's location. See Table 2 in Appendix A for color scale.

5.2. Z_{DR} Column and K_{DP} Column

At 23:42:07 a broad Z_{DR} column is seen flanking updrafts A and B, which extends up to at least 4.90 km ARL. The column is defined by values between ~4.5 – ~6.5 dB (Fig. 17). However, the column's magnitude quickly diminishes between 23:50:04 and 23:52:04. Values decrease to between 2.0 – 3.0 dB, with the higher values occurring in the center of the column.

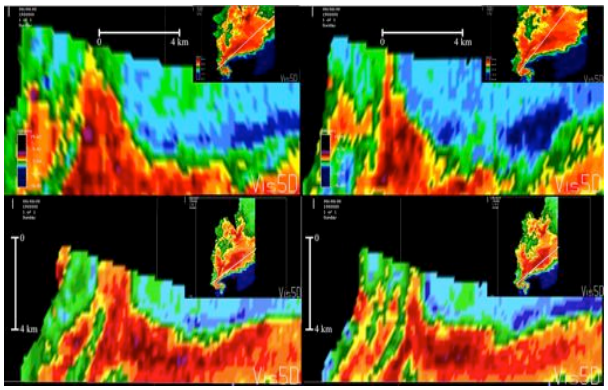

Fig. 17 - Vertical slices indicating the Z_{DR} column adjacent to updraft A. Insets are CAPPIs of Z_H at 1.10 km indicate the location of the slices. Columns are at 23:42:07 (top left), 23:44:04 (top right), 23:46:04 (bottom left), and 23:48:05 (bottom right). Top of the volume is ~4.90 km in height. See Table 2 in Appendix A for color scale.

Also seen between the time period of 23:42:07 and 23:48:05 is a column of K_{DP} in the hook echo indicating the presence of liquid hydrometeors. This is shown in (Fig. 18). K_{DP} values are ~30° km^{-1} to ~45° km^{-1} in the backside of the hook region. This is a region impacted by significant attenuation.

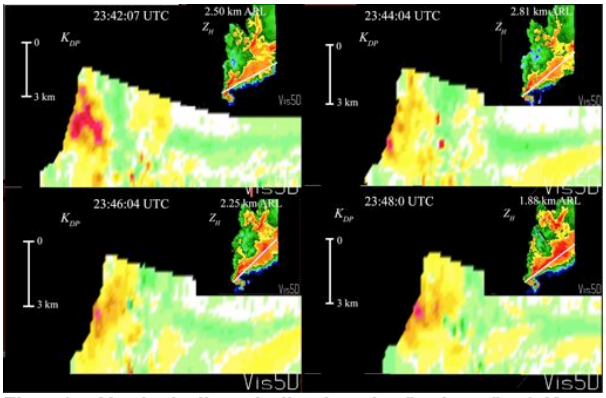

Fig. 18 - Vertical slices indicating the "column" of K_{DP} at 23:42:07 (top left), 23:44:04 (top right), 23:46:04 (bottom left), and 23:48:05 (bottom right). Insets are Z_H CAPPIs at 2.50 km (top left) ARL, 2.81 km (top right) in height, 2.25 km (bottom left) ARL, and 1.88 km (bottom right) ARL. Top of the volume is ~4.90 km ARL. See Table 2 in Appendix A for color scale.

After 22:48:25 there is a narrow Z_{DR} column to the east of the old column's location and to the west of a DRC region (not shown), with values between 4.0 to 6.5 dB. It should be noted that very high Z_{DR} values (between ~3.5 - ~5.5 dB) extend across the entire forward flank of the supercell between 23:58:04 to 00:02:04. The column height exceeds the resolution volume height, because close proximity of the storm limits vertical resolution. Therefore, it is unclear to what height the high Z_{DR} values extend up to. It is expected that the tallest Z_{DR} regions are located along the periphery of the updraft regions.

5.3. Hail Signature

As previously noted, the region flanking updraft A is characterized by low Z_{DR} (~0.5 to ~1.0 dB), low ρ_{HV} (~0.59 to ~0.75), and low Z_H (~25 - ~34 dBZ). It is found on the inflow side of the hook region, and is very consistent with height, and is associated with hail fall. This is a region of low number concentration of larger hail (i.e. the low Z_H region) falling on the periphery of the downdraft region in the hook. At 23:42:20 the hail signature is seen on the southernmost point on the side of the inflow, and is flanked by high Z_H (up to ~62 dBZ), where higher concentrations of hydrometeors are present which are believed to be liquid coated hail. UMXP reported tennis ball and golf ball sized hail in this region at 22:44, which persisted for at least 10 minutes as the storm moved eastward. Up to 2.02 km ARL, Z_H values in the shank of the hook are up to ~62 dBZ. High liquid water content and/or high number concentration are contributing to significant attenuation.

Between 23:44:04 and 23:46:05, hail fall increases to the northeast as seen in (Fig. 19). CAPPIs at various heights indicate fluctuations in Z_{DR}. These fluctuations could be associated with updraft B lofting hail, or it could be horizontal or vertical displacement. Note the dividing

of the Z_{DR} column on the northeast side at 23:44:04 (Fig. 19).

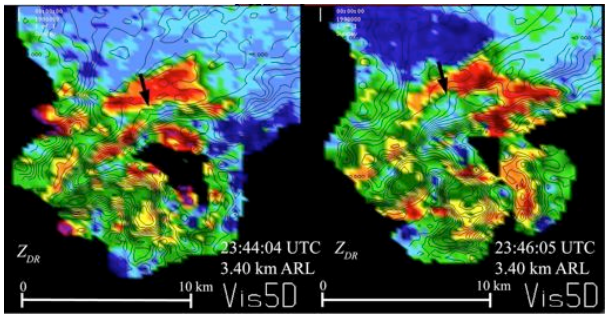

Fig. 19 - Hail signature redistribution as seen in Z_{DR} in CAPPIs at 3.40 km ARL at 23:44:04 (left) and 23:46:05 (right). Z_H is overlaid in black contours every 5 dBZ. The black arrows indicate the hail regime's location. See Table 2 in Appendix A for color scale.

Between 23:44:04 and 23:46:05 the hail corridor descends toward the surface as indicated by the reductions in ρ_{HV} and Z_{DR}. At 23:48:05 Z_H increases with ρ_{HV} between ~0.81 to ~0.84 in the low-levels of the hook, which indicates descending hail. Decreases in ρ_{HV} (~0.90 to ~0.75) indicate the size and/or number concentration of hail is increasing between 23:50:04 and 23:56:04 in both the hook at 0.31 km ARL and along the forward flank as seen in (Fig. 20). UMXP reported ~10.16 cm (4.0 in.) hail at 23:50 in this location. At 23:54:04, ρ_{HV} begins decreasing along the inflow side of the forward flank, and at 23:56:04 ρ_{HV} decreases to ~0.70 to ~0.75. Z_{DR} also drops to ~1.0 to ~2.5 dB in the forward flank, which occurs in a region of Z_H between 35 and 40 dBZ.

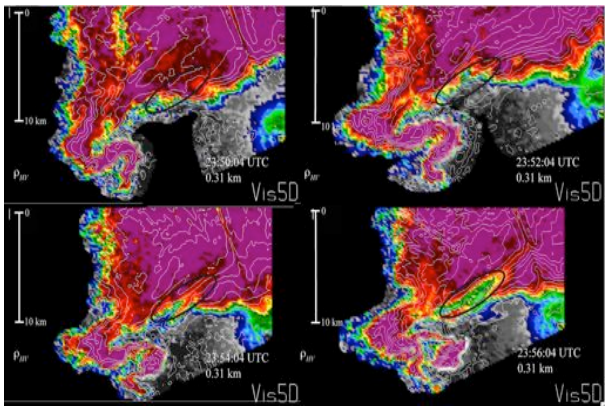

Fig. 20 - CAPPIs taken at 0.31 km in height of ρ_{HV}. Reductions indicate a substantial increase in hail fall between 23:50:04 (top left), 23:52:04 (top right), 23:54:04 (bottom left), and 23:56:04 (bottom right). Overlaid are white contours of Z_H every 5 dBZ. See Table 2 in Appendix A for color scale.

As shown in Fig. 20 at 23:56:04, a "hail corridor" occurs on the leading edge of the forward flank region of the echo around updraft C's location. ρ_{HV} in this region begins to increase above 3.08 km. The DRC region (not shown) looks like small hail down low and pure graupel higher up as Z_H is 30 – 35 dBZ, Z_{DR} is 1.0 to 2.0 dB, and ρ_{HV} is 0.55 – 0.60 at 0.51 km ARL.

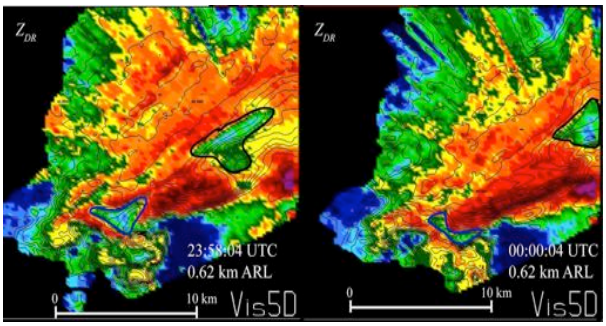

Fig. 21 - CAPPIs at 0.20 km of Z_{DR} at 23:58:04 (left), and at 00:00:04 (right) with eliipses indicating the "hail corridor". White contours are of Z_H at every 5 dBZ. See Table 2 in Appendix A for color scale.

Between 23:58 and 00:02, the narrow Z_{DR} and ρ_{HV} reduction regions move farther east. This is due to the propagation of the storm. This regime is characterized by Z_{DR} ~0.55 to ~2.0 dB, and ρ_{HV} between ~0.70 to ~0.88 at 23:58:04, which weakens by 00:00:04 as seen in CAPPIs at 0.20 km in Fig. 21. This region moved out of the sector by 00:02:04.

Around the melting layer there is sharp gradient seen in ϕ_{DP} immediately behind the corridor of higher Z_{DR} values as seen in Fig. 22. This signature is prominently seen during earlier scans since storm propagation limited the height of observations later on. This signature is similar to the melting layer signature as noted in Melnikov et al. (2005). This region is attributed to significant backscatter differential phase and is believed to be from large liquid coated hail, but concentrated on the back edge of the Z_{DR} corridor and the Z_H core. However, number concentration and particle distributions remain unclear. Beyond this sharp reduction region, minimal Φ_{DP} diminishes attenuation correction. It is important to note that A_H and A_{DP} is still occurring through the heavy core preceding this region. However, Z_H and Z_{DR} beyond this region remain lower than expected as seen in (Fig. 22). The logical explanation would be that this region is dominated by small graupel, ice crystals, or other frozen particles as there are still higher Z_H values beyond this region above the melting layer.

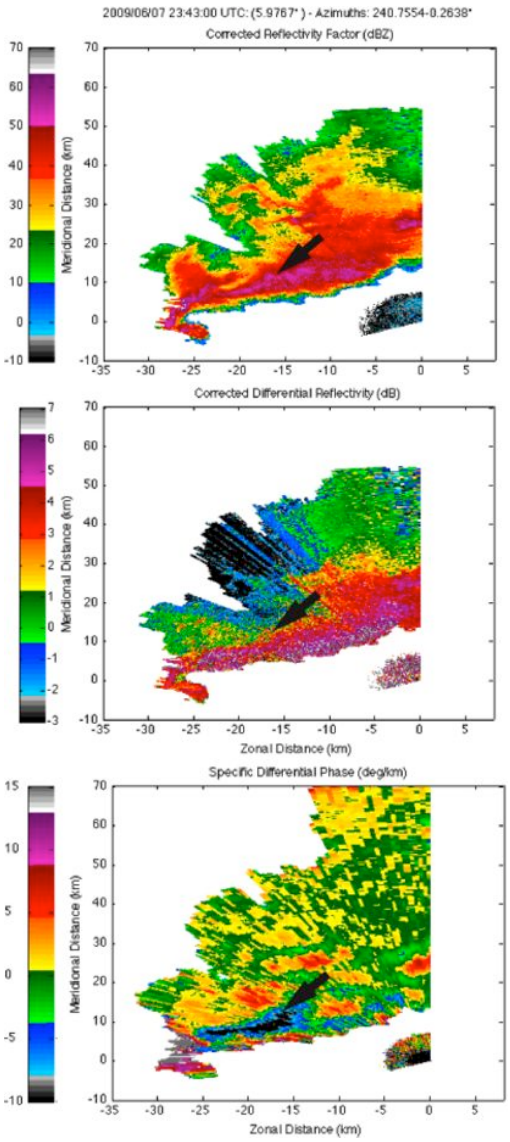

Fig. 22 – PPIs at 6.0° elevation at 23:43 of Z_H (top), Z_{DR} (middle), and K_{DP} (bottom). Significant δ (denoted with black arrow) occurs around the melting layer, which is thought to be liquid coated hail.

5.4. *Z_{DR} Arc Evolution*

A distinct Z_{DR} arc is observed between 23:42:07 and 23:51:46 (Fig. 23). The dark line distinguishes the region of high Z_{DR} values in the arc, which appear to contain larger drops than the arc shown in the 5 June 2009 case. This is not all that surprising given the large concentration of ice hydrometeors within this supercell. Similar to the 5 June case, the arc appears to fluctuate through its lifetime (Fig. 23). It remains unclear, but perhaps the unusual progression of updrafts along the forward flank led to the demise of the arc. Furthermore, a broad region of high Z_{DR} values persists in the FFC well after the arc's demise at ~23:52.

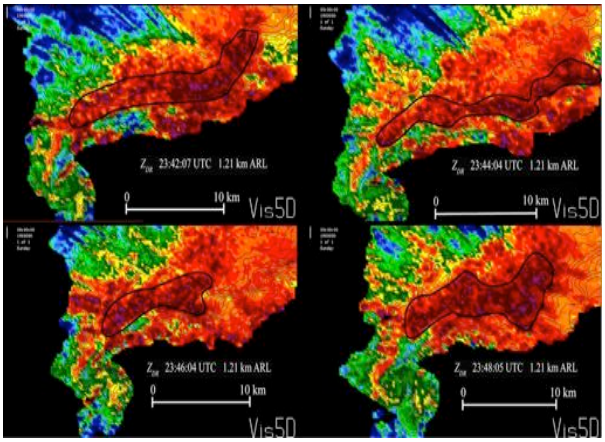

Fig. 23 - Z_{DR} CAPPIs taken at 1.21 km ARL at 23:42:07 (top left), 23:44:04 (top right), 23:46:04 (bottom left), and 23:48:05 (bottom right). The black line indicates the Z_{DR} arc region. See Table 2 in Appendix A for color scale.

6. 10 MAY 2010

On 10 May 2010, NOXP deployed at 23:34 on a cyclic, tornadic supercell. A tornado was ongoing, and WSR-88D data from KTLX indicated a left-moving cell moving towards the supercell. The terrain blocked the 1° elevation and partially blocked the 2° and 3° elevations. At 23:42, UMXP deployed for dual-Doppler data collection, which is detailed in Burgess et al (2011). Initially the storm was ~15 km from NOXP, but fast-storm motion (~15-20 m/s) and limited heights of observation hamper the analyses of the dual-polarimetric signatures. Given these limitations, the dual-pol analysis will focus on the storm merger; hook echo development, an occlusion downdraft signature, and a brief discussion of attenuation limitations. Local soundings indicate the freezing level is ~3.65 km ARL. Close spatial proximity to the echo initially limit observation heights to ~1.84 km ARL.

6.1. Storm Merger Properties

A large rain wrapped tornado is ongoing during the start of the NOXP deployment. This is evident in a large rain-filled hook, which is evident by moderate Z_{DR} (~1.55 - ~3.50 dB), high ρ_{HV} (~0.95 - ~0.98 surrounding the TDS), and increasing Z_H (~40 - ~60 dBZ) with respect to height. The merging left mover, composed moderate sized drops (Z_{DR} between ~2.4 - ~4.4 and ρ_{HV} between ~0.95 - ~0.98, entrains cyclonically into the circulation (Fig. 24). The increase in liquid water content increases attenuation through the hook, and K_{DP} increases with height (up to ~40° km^{-1}). The merger/entrainment of the left-mover's precipitation likely has increased drop sizes, but appeared to not affect the mesocyclone/tornado. A tornadic debris signature is evident in ρ_{HV} (~0.85 to ~0.93) at 1.70 km ARL (Fig. 25) between ~23:36 to ~23:42. The high liquid water content within the

circulation is likely to enhance ρ_{HV} as seen here from wet debris and/or a mixture of rain and debris.

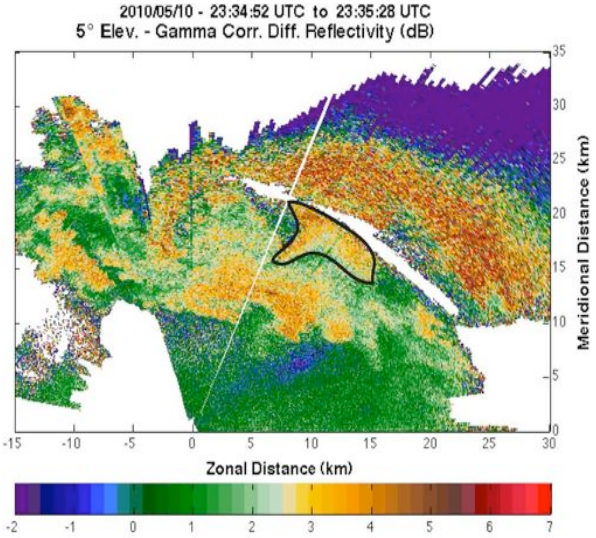

Fig. 24 - PPI at 5.0° in elevation during the 23:34:00 volume scan. The black outline indicates the band of descending moderate sized raindrops that is advecting in towards the circulation.

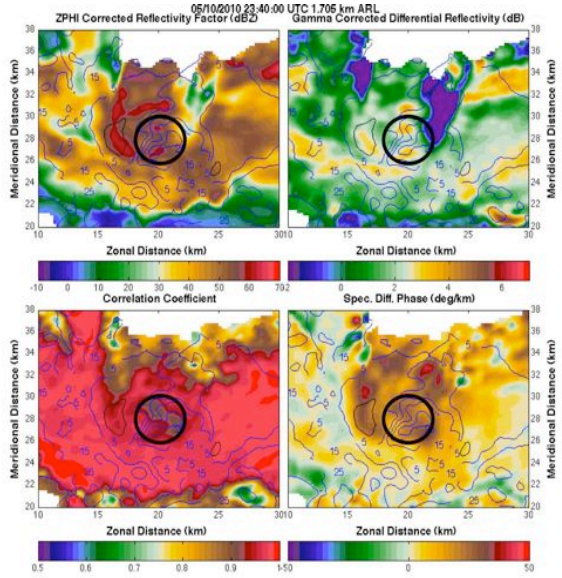

Fig. 25 - CAPPIs at 23:40 of Z_H (top left), Z_{DR} (top right), ρ_{HV} (lower left), and K_{DP} (lower right) at ~1.70 km ARL illustrating the TDS (black circle), which is distinctly seen in ρ_{HV} despite the significant amount of liquid in the circulation (as noted in K_{DP} and Z_{DR}). Black (blue) contours are inbound (outbound) radial velocity.

6.2. Limitations on Dual-Pol Quality

A significant amount of attenuation occurs through the hook echo and the core of this supercell throughout its lifetime. Attenuation corrections return much of the Z_H field, but negative Z_{DR} values remain. Furthermore, a significant amount of NBF occurs in regions of sharp gradients of Z_H and/or Φ_{DP} (Fig. 26). This renders ρ_{HV} and other dual-pol variables useless in these regions limiting capabilities of drawing conclusions about hail.

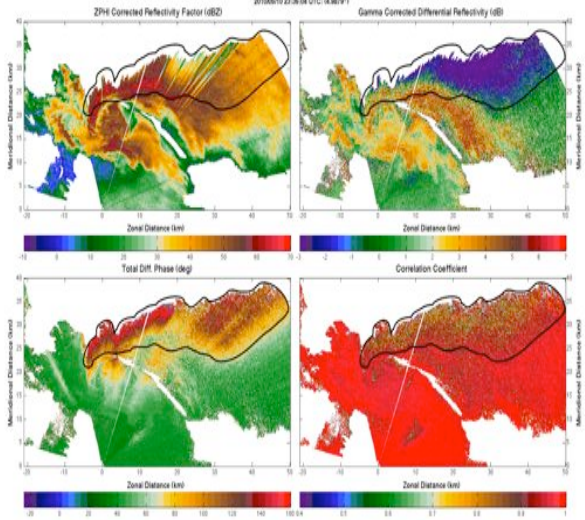

Fig. 26 - Regions outlined are impacted by strong A_{DP} (noted by remnant negative Z_{DR} (top right)), which has led to NBF as noted with the reductions of ρ_{HV} (lower right). Sharp gradients in Φ_{DP} (bottom left) result in NBF. This PPI elevation scan is at 5.0° elevation at 23:35:04.

Furthermore, height limitations of data and the storm merger in the forward flank at ~23:40 limit observations of Z_{DR} columns. However, from the start of the deployment and prior to the merger at ~23:40, a well-defined Z_{DR} arc is seen extending towards the circulation (Fig. 27).

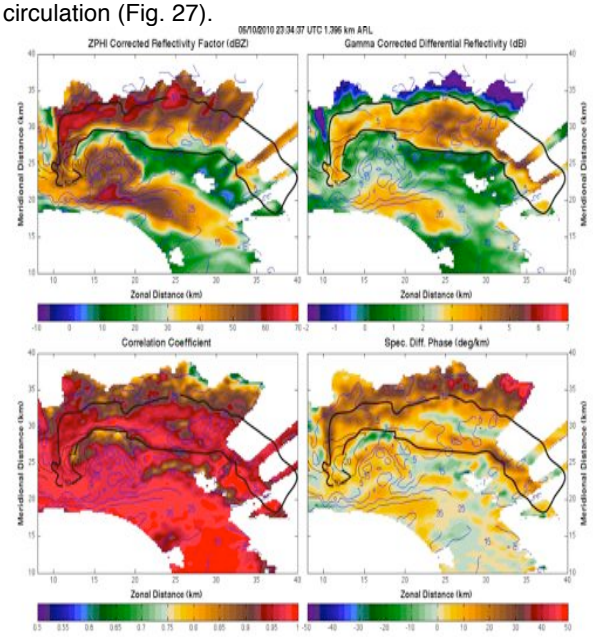

Fig. 27 - CAPPIs of Z_H (top left), Z_{DR} (top right), ρ_{HV} (lower left), and K_{DP} (lower right) at ~1.40 km ARL. These CAPPIs are seen at 23:34. The Z_{DR} arc is outlined by the black contour. Overlaid in black (blue) contours are inbound (outbound) radial velocities.

6.3. Hook Echo Development and Occlusion Downdraft

Similar to Beck et al. (2006), hook echo development from cyclic mesocyclogensis is observed in this particular supercell. As detailed in Burgess et al. (2011), the hook develops in a zone of strong confluent flow between the old circulation and the developing circulation. This confluence horizontally and vertically advects precipitation into the region between the two circulations. It is hypothesized that this axis of dilatation is responsible for the narrowness of the hook echo at 23:46 (Fig. 28). Despite the loss of power-based variables Z_H and Z_{DR} from beam blockage at low-levels, the phase-based variable K_{DP} distinguishes the developing hook echo (Fig. 29). Curiously, with increasing height and time K_{DP} exceeds 45° km^{-1}, ρ_{HV} exceeds 0.95, Z_{DR} is fairly moderate (~1.8 – ~3.0 dB), and Z_H (50 – 65 dBZ) remains high. These values of K_{DP} exceed the theoretical limit for X-Band as shown in T-matrix calculations from Snyder et al. (2010). Thus, uncertainty remains about the plausibility of K_{DP}, but resonance impacts (perhaps from melting hail) are most certainly impacting these measurements. However, high ρ_{HV} suggests a high likelihood of a purely liquid hydrometeor medium.

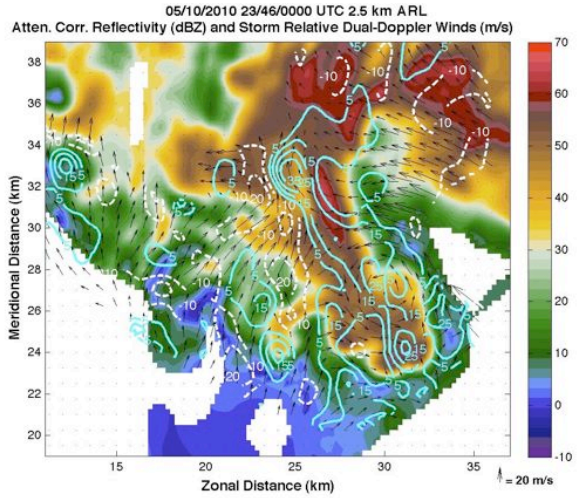

Fig. 28 – CAPPI of Z_H at 2.5 km ARL during the 23:46 volume scan of NOXP and UMXP. The dual-polarimetric data are taken from NOXP. Contours are of vertical velocity (*w* [m s-1]) and vectors (every third vector is plotted) indicate the storm relative velocities [m s^{-1}] as estimated through the dual-Doppler wind synthesis. Note the narrowing precipitation hook echo from the confluent flow.

Another unique signature observed in the dual-Doppler during the cyclic process is that of the occlusion downdraft (e.g., Klemp and Rotunno 1983), which is also discussed in more detail in Burgess et al. (2011). The occlusion downdraft is first observed aloft at 23:42, and is distinguished by lower Z_H (~26 to ~28 dBZ), lower Z_{DR} (~1.8 to ~2.0 dB), lower ρ_{HV} (~0.87 to ~0.90), and negative K_{DP} (~-2.5 – 0° km^{-1}) (Fig. 30). This signature lowers in height with time, and after 22:44 no longer remains. However, uncertainty remains about the diabatic contributions (i.e., evaporational cooling) to the downdraft and the dynamic forcing contributions to the downdraft.

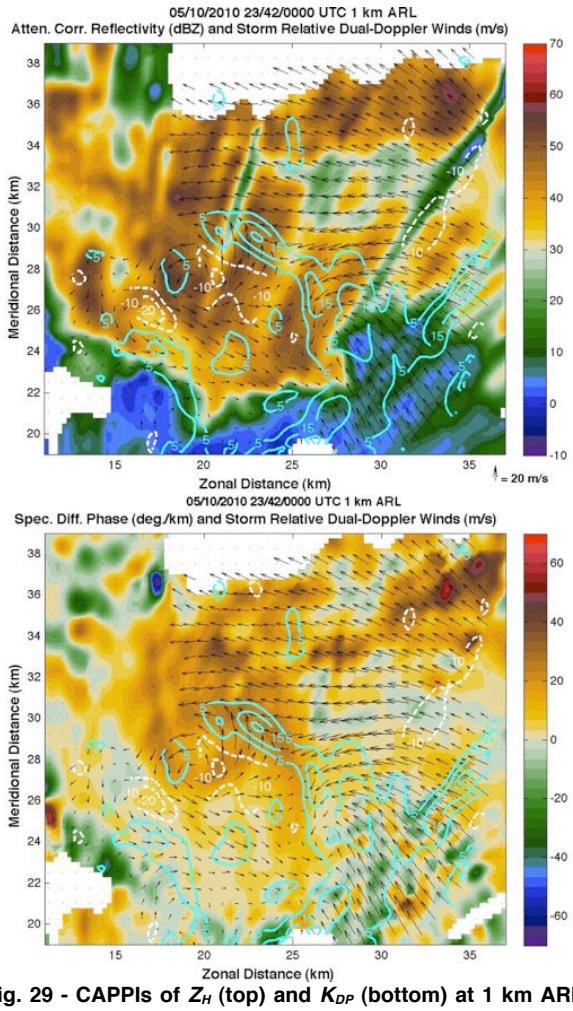

Fig. 29 - CAPPIs of Z_H (top) and K_{DP} (bottom) at 1 km ARL during the 23:42 volume scan of NOXP and UMXP. All contours and vectors are the same as Fig. 28. Note the use of K_{DP} in the regions of partial beam blockage (as shown in Z_H).

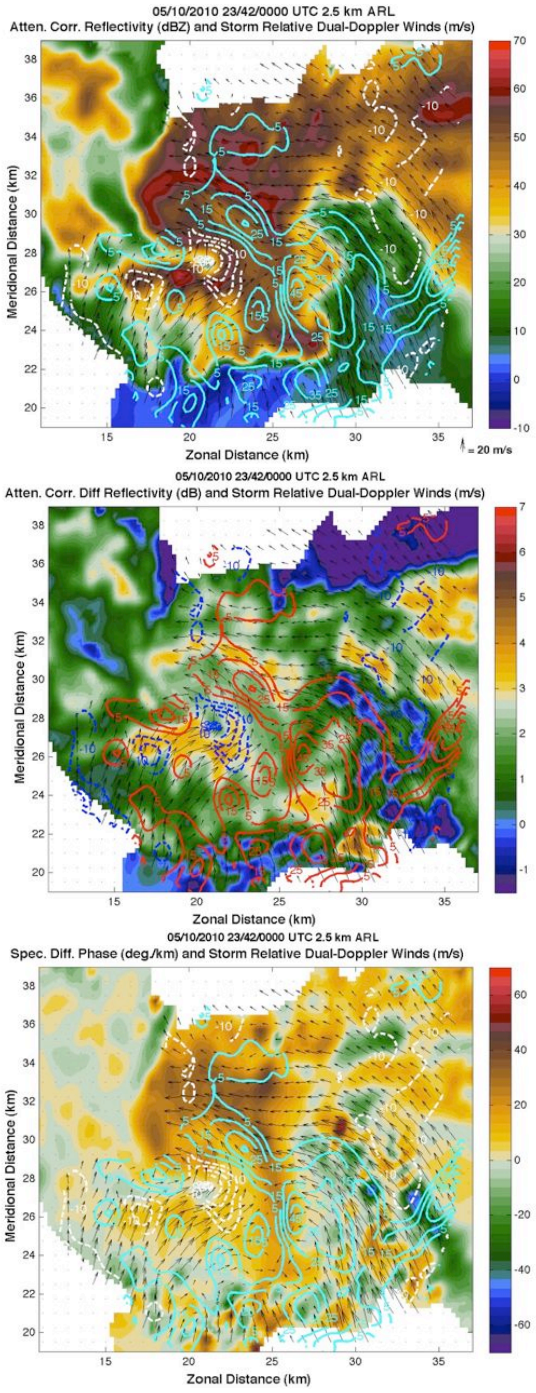

Fig. 30 - CAPPIs of Z_H (top), Z_{DR} (middle), and K_{DP} (bottom) at 2.5 km ARL during the 23:42 volume scan of NOXP and UMXP. All contours and vectors are the same as Fig. 28. Note the dual-pol signature, which coincides with the occlusion downdraft as shown in the *w* field.

SUMMARY

Data collected by NOXP on three supercells have been examined. Attenuation corrections using the ZPHI Rain-Profiling Algorithm and/or the Gamma method are applied. Two of the supercells were strongly tornadic (5 June 2009 and 10 May 2010), and one of which was non-tornadic (7 June 2009). Both 2009 storms produced large hail. 5 June progressed as a more classic supercell with diminishing hail size as time elapsed, and 7 June became an outflow dominant high precipitation supercell. A tornadic vortex signature (TVS) is seen in the early stages of 5 June, but limitations, such as the dropout of ρ_{HV} in the vicinity of the tornado's location, and wide gate width limit the capability of verifying the presence of a tornado debris signature (TDS). Another TDS is seen in 10 May, but with higher ρ_{HV}, which is likely due to precipitation entrainment from a merging left mover. The merging left-mover did not appear to influence the mesocyclone/tornado otherwise. Cyclic evolution of the updraft is seen in Z_H often between ~25 – ~30 dBZ, Z_{DR} between ~ -0.6 to ~1.5 dB, and ρ_{HV} ranging from >0.4 to ~0.85 in the 5 June and 7 June cases. These values do vary some in time, but are characteristic of the type of scatterer in the updraft.

A unique hail signature is seen with variable Z_H often between ~30 - ~65 dBZ, low Z_{DR} between ~0 dB to ~2.5 dB, and ρ_{HV} ranging from ~0.25 to ~0.85 in both the June 5 and June 7 cases. Number concentration, hydrometeor type, and diameters are seen to impact these values in both storms. In both storms, there appears to be a "hail corridor" region, but is found in different locations for each storm. 5 June's "hail corridor" is located north of the hook echo extending well into the forward flank. 7 June's "hail corridor" is found just on the inflow side of the shank of the hook, and later on along the leading edge of the forward flank region. Non-uniform beam filling and attenuation limit the conclusions of hail observations for the 10 May 2010 case.

Z_{DR} columns are seen to rapidly correlate to the onset of a new updraft with values up to 6.5 dB in the 5 and 7 June cases, but data limitations prevented observations of Z_{DR} columns in the 10 May case. However, in all three storms, K_{DP} columns are most commonly seen in the location of the hook echo. This could be influenced by the amount of backscatter differential phase δ present in the forward flank regions masking the K_{DP} columns there. Limitations due to storm proximity limit observations of the column's top on 7 June. A well-defined Z_{DR} arc is found in the 5 June and 7 June cases, both of which tend to oscillate with time. An arc is observed in the 10 May case up to the point of a storm merger. Similar to updraft evolution, the Z_{DR} arc evolves on time scales much faster than were sampled. Thus higher temporal resolution is required for further investigation of these signatures. No distinctive Z_{DR} or ρ_{HV} rings were observed in any of the cases.

In the 10 May case, despite low-level beam blockage, K_{DP} distinguishes the development of a hook echo during cyclic mesocyclogensis. Confluent flow is likely responsible for not only hook echo development, but also its narrow and elongated characteristics. Furthermore, high K_{DP}, ρ_{HV}, Z_H, and moderate Z_{DR} suggest a purely liquid hydrometeor medium. However,

resonance impacts are likely yielding anomalously high K_{DP}. Lastly, the occlusion downdraft reveals a unique signature in Z_H, K_{DP}, ρ_{HV}, and Z_{DR}. Z_H drops as low as ~26 to ~28 dBZ, Z_{DR} down to ~1.8 to ~2.0 dB, ρ_{HV} from ~0.87 to ~0.90, and K_{DP} between ~-2.5 – 0° km^{-1}.

APPENDIX A

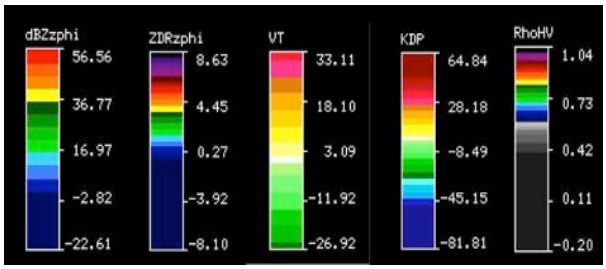

Table 2 - Color scales for each of the radar variables from the 5 June and 7 June 2009 data sets as seen in the *Vis5D* visualization software package.

ACKNOWLEDGEMENTS

We would like to thank Jeff Snyder for allowing the use of his attenuation correction program. We would also like to thank the NSSL/CIMMS engineers who maintain the NOXP mobile weather radar. We would also like to thank Matt Kumjian for his assistance with interpretation of the dual-polarization data, Mike Buban with his assistance in adapting the Barnes objective analysis scheme, and Yvette Richardson at Penn State for supplying dual-Doppler data for the 5 June case. Funding for this study comes from NSF Grant ATM-0802717 and NOAA-University of Oklahoma Cooperative Agreement #NA17RJ1227.

REFERENCES

Barnes, S.L., 1964: A technique for maximizing details in numerical weather map analysis. *J. Appl. Meteor.*, **3,** 396-409.

Bringi, V.N., V. Chandrasekar, N. Balakrishnan, and D.S. Zrnic, 1990: An examination of propagation effects in rainfall on radar measurements at microwave frequencies. *J. Atmos. Oceanic Technol.*, **7,** 829-840.

Bringi, V.N., and Chandrasekar, 2001: *Polarimetric Droppler Weather Radar: Principles and Applications.* Cambridge University Press, 636 pp.

Bringi, V.N., T.D. Keenan, and V. Chandrasekar, 2001: Correcting C-band radar reflectivity and differential reflectivity data for rain attenuation: A self-consistent method with constraints. *IEEE Trans. Geosci. Remote Sens.*, **39,** 1906-1915.

Brown, R.A., 1992: Initiation and evolution of updraft rotation within an incipient supercell thunderstorm. *J. Atmos. Sci.*, **49,** 1997-2014.

Burgess, D.W., C.M. Schwarz, J.C.Snyder, M.M. French, and H.B. Bluestein, 2011: A cyclic, tornadic supercell from 10 May 2010: Analysis of a VORTEX2 case. Preprints, *35th Conf. on Radar Meteorology,* Pittsburgh, PA, Amer. Meteor. Soc., 8B.4.

Cao, Q., G. Zhang, E. Brandes, T. Schuur, A. Ryzhkov, and K. Ikeda, 2008: Analysis of video disdrometer and polarimetric radar data to characterize rain microphysics in Oklahoma. *J. Appl. Meteor. Climat.,* **47,** 2238-2255.

Cao, Q., and G. Zhang, 2009: Errors in estimating raindrop size distribution parameters: A study based on simulation and real data. *J. Appl. Meteor. Climat.,* **48,** 406-425.

Caylor, I., and A.J. Illingworth, 1987: Radar observations and modeling of warn rain initiation. *Quart. J. Roy. Meteor. Soc.,* **113,** 1171-1191.

Davies-Jones, R. D.W. Burgess, and M. Foster, 1990: Test of helicity as a forecast parameter. Preprints, *16th Conf. on Severe Local Storms*, Kananaskis Park, Alberta, Canada, Amer. Meteor. Soc., 588-592.

Doviak, R.J., and D.S. Zrnic, 1993: *Doppler Radar and Weather Observations.* Academic Press, 562 pp.

Fankhauser, J. C., 1971: Thunderstorm environment interactions determined from aircraft and radar observations. *Mon. Wea. Rev.*, **99,** 171-192.

Fujita, T., 1965: Formation and steering mechanisms of tornado cyclones and associated hook echoes. *Mon. Wea. Rev.*, **93,** 67-78.

Heinselman, P.L., and A.V. Ryzhkov, 2006: Validation of polarimetric hail detection. *Weather and Forecasting*, **21,** 839-850.

Hitschfeld, W., and J. Bordan, 1954: Errors inherent in the radar measurement of rainfall at attenuation wavelengths. *J. Atmos. Sci.,* **11,** 58-67.

Höller, H., V.N. Bringi, J. Hubbert, M. Hagen, and P.F. Meischner, 1994: Life cycle and precipitation formation in a hybrid-type hailstorm revealed by polarimetric and Doppler radar measurements. *J. Atmos. Sci.*, **51,** 2500-2522.

Hubbert, J., and V.N. Bringi, 1995: An iterative filtering technique for the analysis of the copolar differential phase and dual-frequency radar measurements. *J. Atmos. Oceanic Technol.*, **12,** 643-648.

Hubbert, J., V.N. Bringi, L.D. Carey, and S. Bolen, 1998: CSU-CHILL polarimetric measurements from a severe hailstorm in eastern Colorado. *J. Appl. Meteor.*, **37,** 749-755.

Jameson, A.R., 1991: Polarization radar measurements in rain at 5 and 9 GHz. *J. Appl. Meteor.*, **30,** 1500-1513.

Jameson, A.R., 1992: The effect of temperature on attenuation-correction schemes in rain using polarization propagation differential phase shift. *J. Appl. Meteor.*, **31,** 1106-1118.

Kennedy, P.C., S.A. Rutledge, W.A. Petersen, and V.N. Bringi, 2001: Polarimetric radar observations of hail formation. *J. Appl. Meteor.*, **40,** 1347-1366.

Klemp, J.B., and R. Rotunno, 1983: A study of the tornadic region within a supercell thunderstorm. *J. Atmos. Sci.*, **40,** 359-377.

Koch, S.E., M. desJardins and P.J. Kocin, 1981: The GEMPAK Barnes objective analysis scheme. NASA Tech. Memo. ERL NSSL-51

Kumjian, M.R., 2008: Polarimetric radar analysis of microphysical processes in supercell storms. M.S. Thesis, University of Oklahoma, 188 pp. [Available from School of Meteorology, University of Oklahoma, 120 David L. Boren Blvd., Norman, OK 73072]

Kumjian, M.R., and A. V. Ryzhkov, 2008: Polarimetric signatures in supercell thunderstorms. *J. Appl. Meteor. and Climatology*, **48,** 1940-1961.

Kumjian, M.R., and A. V. Ryzhkov, 2009: Storm relative helicity revealed from polarimetric radar measurements. *J. Atmos. Sci.*, **66,** 667-685.

Kumjian, M.R., A. V. Ryzhkov, V. M. Melnikov, and T. J. Schuur, 2010: Rapid-scan super- resolution observations of cyclic supercell with a dual-polarization WSR-88D. *Mon. Wea. Rev.*, **138,** 3762-3786.

Loney, M.L., D.S. Zrnic, J.M. Straka, and A.V. Ryzhkov, 2002: Enhanced polarimetric radar signatures above the melting layer in a supercell storm. *J. Appl. Meteor.*, **41,** 1179-1194.

Majcen, M., P. Markowski, Y. Richardson, D. Dowell, and J. Wurman, 2008: Multipass objective analyses of Doppler radar data. *J. Atmos. Oceanic Technol.*,**25,** 1845-1858.

Matrosov, S.Y., K.A. Clark, B.E. Martner, and A.Tokay, 2002: X-band polarimetric radar measurements on rainfall. *J. Appl. Meteor.* , **41,** 941-952.

Melnikov, A.V., V.M. Melnikov, and A.V. Ryzhkov, 2005: On the differential phase in the melting layer. Extended Abstracts, *32nd Conference on Radar Meteorology/11th Conference on Mesoscale Processes*, Albuquerque, NM, Amer. Meteor. Soc., P9R.9.

Newton, C.W., and H. R. Newton, 1959: Dynamical interactions between latge convective clouds and environmental vertical shear. *J. Meteor.*, **16,** 483-496.

Outinen, K. and J. Teittinen, 2007: Case study of a tornadic supercell in Finland 28 August 2005. *Proc. Fourth European Conf. on Severe Storms,* Trieste, Italy, International Centre for Theoretical Physics, 05.14.

Oye, R., C.K. Mueller, and S. Smith, 1995: Software for radar translation, visualization, editing, and interpolation. Preprints, *27th Conference on Radar Meteorology*, Vail, CO, American Meteorological Society, 359-361.

Park, S.G., V.N. Bringi, V. Chandrasekar, M. Maki, and K. Iwanami, 2005: Correction of radar reflectivity and differential reflectivity for rain attenuation at X band. Part I: Theoretical and empirical basis. *J. Atmos. Oceanic Technol.*, **22,** 1621-1632.

Ray, P. S., C. L. Ziegler, and W. Bumgarner, and R. Serafin, 1980: Single- and multi-Doppler radar observations of tornadic storms. *Mon. Wea. Rev.,* **108,** 1607-1625.

Romine, G.S., D.W. Burgess, and R.B. Wilhelmson, 2008: A dual-polarization-radar-based assessment of the 8 May 2003 Oklahoma City area tornadic supercell. *Mon. Wea. Rev.,* **136,** 2849-2870.

Ryzhkov, A.V., 2007: The impact of beam broadening on the quality of radar polarimetric data. *J. Atmos. Oceanic Technol.,* **24,** 729-744.

Ryzhkov, A.V., D. Burgess, D. Zrnic, T. Smith, and S. Giangrande, 2002: Polarimetric analysis of a 3 May 1999 tornado. Preprints, *22nd Conf. onSevere Local Storms*, Hyannis, MA, Amer. Meteor. Soc., 14.2. [Available online at http://ams.confex.com/ams/pdfpapers/95684.pdf]

Ryzhkov, A.V., T. J. Schuur, D. W. Burgess, and D. S. Zrnic, 2005: Polarimetric tornado detection. *J. Appl. Meteor.*, **44,** 557-570.

Ryzhkov, A.V., and D.S. Zrnic, 1995: Precipitation and attenuation measurements at a 10-cm wavelength. *J. Appl. Meteor.*, **34,** 2121-2134.

Ryzhhkov, A.V., and D.S. Zrnic, 2005: Radar polarimetry at S, C, and X bands. Comparitive analysis and operational implications. Extended Abstracts, *32nd Conf. on Radar Meteorology*, Albequerque, NM, Amer. Meteor. Soc., 9R.3.

Snyder, J.C., 2008: Attenuation correction techniques and hydrometeor classification of high-resolution, X-band, dual-polarized mobile radar data of sever convective storms. M.S. Thesis, University of Oklahoma, 148 pp. [Available from School of Meteorology, Unviersity of Oklahoma, 120 David L. Boren Blvd., Norman, OK 73072].

Snyder, J.C., H. B. Bluestein, G. Zhang, and S. J. Frasier, 2010: Attenuation correction and hydrometeor classification of high-resolution, X-band, dual-polarized mobile radar measurements in severe convective storms. *J. Atmos. Ocean. Technology.*, **27,** 1979-2001.

Testud, J., E.Le Bouar, E. Obligis, and M. Ali-Mehenni, 2000: The rain profiling algorithm applied to polarimetric weather radar. *J. Atmos. Oceanic Technol.*, **17,** 332-356.

Van Den Broeke, M.S., J.M. Straka, and E.N. Rasmussenm 2008: Polarimetric radar observations at low levels during tornado life cycles in a small sample of classic Southern Plains supercells. *J. Appl. Meteor. Climatol.*, **47,** 1232-1247.

Zrnic, D. S., and A. V. Ryzhkov, 1999: Polarimetry for weather surveillance radars. *Bull. Amer. Meteor. Soc.,* **80,** 389-406.